Controlling Oriented Attachment and *In Situ* Functionalization of TiO_2 Nanoparticles During Hydrothermal Synthesis with APTES

Antoine R. M. Dalod,[†] Ola G. Grendal,[†] Susanne L. Skjærvø,[†] Katherine Inzani,[†] Sverre M. Selbach,[†] Lars Henriksen,[‡] Wouter van Beek,[‖] Tor Grande,[†] Mari-Ann Einarsrud[†,]*

[†] Department of Materials Science and Engineering, NTNU, Norwegian University of Science and Technology, 7491 Trondheim, Norway

[‡] poLight AS, Kongeveien 77, 3188 Horten, Norway

[‖] Swiss-Norwegian Beamlines at European Synchrotron Research Facility, 38043 Grenoble, France

* Corresponding author: Mari-Ann Einarsrud

Email address: mari-ann.einarsrud@ntnu.no

Telephone: +47 73 59 40 02

ABSTRACT

Understanding growth mechanisms and the role of surface functionalization is of key importance to control shape and morphology of nanoparticles and their properties. Here, we describe the growth mechanism and the effect of hydrothermal synthesis parameters (pH, time and precursor/functionalization agent ratio) during *in situ* functionalization of anatase TiO_2 nanoparticles with 3-aminopropyltriethoxysilane. Elongated crystallographically oriented TiO_2 nanoparticles were formed by oriented attachment mechanism in addition to spherical nanoparticles. The growth mechanism is determined by a combination of *ex situ* techniques such as high-resolution transmission electron microscopy combined with *in situ* synchrotron X-ray diffraction and density functional theory calculations. Oriented attachment induced by the functionalization agent is shown to be the origin of the elongation of the nanoparticles, as only spherical nanoparticles were formed in the absence of surface functionalization. Finally, it was shown that the amount and the size of the elongated nanoparticles can be tuned by adjusting pH.

1. INTRODUCTION

Controlling the particle size, morphology, and crystallinity (including the type of polymorph) of titanium dioxide (TiO_2) nanoparticles has attracted a lot of interest with respect to tailored materials dedicated to applications such as in the energy or in the biomedical fields.[1, 2] With respect to controlling these parameters, solvothermal and hydrothermal syntheses[3] are intensively investigated in order to obtain efficient anatase TiO_2 nanomaterials for *e.g.* photocatalysis[4, 5] and photovoltaics,[6] but also because of the intrinsic advantages of the method, simplicity and cost efficiency.[7] Surface functionalization of nanoparticles with organic molecules such as silane coupling agents,[8-12] brings additional properties and better dispersion in organic solvents and polymers.[12-15]

The effect of the synthesis conditions on the morphology of TiO_2 nanoparticles has been the focus of numerous works. Dinh *et al*. studied solvothermal synthesis of anatase TiO_2 in ethanol reporting different shapes such as rhombic, truncated rhombic, spherical, and dog-bone, by tuning the oleic acid and oleylamine surfactants molar ratio.[16] Correspondingly, Jun *et al.* tuned the surface selective surfactant (lauric acid) and the surface nonselective surfactant (trioctylphospine oxide) during non-hydrolytic synthesis of TiO_2 nanoparticles, leading to morphologic evolution from spheres to diamond, rod, and branched rod shapes.[17] In both reports, the anatase nanoparticles were elongated along the [001] direction. Anisotropic growth of TiO_2 nanoparticles synthesized by solvothermal reaction of $TiCl_4$ in benzyl alcohol was also reported.[18] Recently, asparagus, wire, cube, eggplant, and tetragon shapes were obtained via solvothermal synthesis in cyclohexane.[19] Elongation along [001] direction was considerably reduced with addition of sodium oleate; from which it was deduced that it strongly adsorbs on {001} facets. Sugimoto *et al*. observed a change from cube shaped to ellipsoidal shape of TiO_2 nanoparticles synthesized via a combination of sol-

gel and hydrothermal treatments, using triethanolamine as surface selective surfactant and pH above 11.[20] Similar effects were observed using different primary amines.[21] Li *et al.* reported a combined solvothermal/hydrothermal synthesis with tunable shapes of anatase nanoparticles from spherical to rod-like shapes, elongated along the [101] direction, as a function of the increasing temperature.[4] Oriented attachment is now a well-known phenomenon in which nanoparticles self-organize spontaneously, sharing a common crystallographic plane and resulting in monocrystalline particles.[22, 23] Oriented attachment of anatase nanoparticles to form [001] elongated nanoparticles has been observed in earlier studies.[24-26]

We have previously reported an *in situ* hydrothermal route to functionalize TiO_2 nanoparticles with silane coupling agents.[27] While spherical nanoparticles were observed in the case of pure TiO_2 and TiO_2 *in situ* functionalized with *n*-decyltriethoxysilane, [001] oriented rods were also formed along with spheres in the case of functionalization with aminosilanes. We proposed that the formation of the rods was due to a combination of specific adsorption or surface selective adsorption of the aminosilane and oriented attachment mechanism, as the functionalization and the growth occur simultaneously, and both spheres and rods were formed.

Here we report on the growth mechanism of elongated particles and the role of the surface functionalization during hydrothermal synthesis with focus on *in situ* functionalization of TiO_2 with 3-aminopropyltriethoxysilane (APTES). We applied a unique combination of *in situ* X-ray diffraction during the hydrothermal synthesis and *ex situ* studies on the process parameters influencing the formation of rod-like nanoparticles to determine the growth mechanism of the [001] oriented nanoparticles. The simultaneous growth and functionalization of the anatase TiO_2 nanoparticles are discussed with particular attention to the role of the surface functionalization on

the phase purity and the morphology of the nanoparticles. The conclusions on the growth mechanism were supported by density functional theory calculations.

2. METHODS

2.1 Synthesis

The syntheses were based on the *in situ* functionalization of TiO_2 nanoparticles with silane coupling agents as previously described,[27] using titanium(IV) isopropoxide (TIP, Sigma-Aldrich, ≥ 97 %) as titanium precursor and APTES (Sigma-Aldrich, 99 %) as functionalization agent. TIP (28 mmol) was added to distilled water and APTES (TIP:APTES molar ratio equal to 10:1 and 15:1) to obtain a filling factor of 70 % in the autoclave. The solutions were stirred for 10 min prior to transfer into a 125 mL PTFE-lined autoclave (Parr) and heated for selected duration time (1, 15, 30, 60 and 120 min) at 200 °C. After cooling to room temperature, the products were centrifuged (10000 rpm, 10 min) and washed with distilled water. This process was repeated 3 times. The obtained slurries were dried for about 12 h at 100 °C for analysis. The effect of changing the pH was investigated for the 120 min synthesis time using ammonium hydroxide (Sigma-Aldrich, 30-33 %) and nitric acid (Sigma-Aldrich, 65 %) to give pH values of about 10 and 2, respectively. Table 1 summarizes the synthesis conditions and the labels of the samples.

The slurries used for *in situ* X-ray diffraction (XRD) measurements were prepared three times more concentrated than the synthesis in autoclave in order to obtain a good diffraction signal during the acquisition. Typically, 9.55 mmol of TIP was added to distilled water to get a total volume of 10 mL. When the synthesis was performed to produce *in situ* functionalized TiO_2 with APTES, the necessary volume of water is substituted to APTES. The temperature and the pressure were 213 °C and 250 bar, respectively, for all *in situ* experiments.

Table 1. Sample names and parameters of the 120 min hydrothermal synthesis of TiO_2 and APTES *in situ* functionalized TiO_2 nanoparticles.

Sample name	TIP:APTES (mol. ratio)	pH	*In situ* XRD
TiO_2-A	n/a	2.7	No
TiO_2	n/a	4.5	Yes[a]
TiO_2-B	n/a	9.3	No
10:1-A	10:1	2.2	No
10:1	10:1	6.3	Yes[a]
10:1-B	10:1	10.1	Yes[b]
15:1-A	15:1	2.2	No
15:1	15:1	6.3	No
15:1-B	15:1	9.7	No

[a] pH was not measured and not modified.

[b] pH was increased to about 10 with ammonium hydroxide.

2.2 Computational

Density functional theory (DFT) calculations were performed using the Vienna *ab initio* Simulation Package (VASP) with projector augmented wave (PAW) pseudopotentials, the exchange-correlation functional PBEsol and an energy cut-off of 700 eV.[28-32] A slab model was employed for calculation of (001), (100) and (101) surface energies and binding energies with single-sided absorption of APTES. Meroni *et al*. investigated the geometrical configuration of APTES on the fully hydroxylated (101) anatase surface by a combined experimental and theoretical study, finding that single molecules or dimers could chemisorb with feasible geometries but high bond strain limited extensive crosslinking.[33] Adsorption was modelled via Ti–O–Si

bonding to 25 % hydroxylated surface Ti, with removal of one C_2H_5 branch from the APTES molecule. This situation can be considered as an intermediate stage of the reaction. More computational details are given in the supporting information.

2.3 Characterization

Powder X-ray diffraction (XRD) was performed on a Bruker D8 Advance Da-Vinci working in Bragg-Brentano (θ/2θ) geometry and equipped with LynxEye detector. Diffractograms were recorded with CuK_α radiation (λ = 1.5406 Å), with a step size of 0.013°, an integration time of 0.4 s, and using variable divergent slits. The *in situ* XRD measurements were carried out at the Swiss-Norwegian Beamlines (BM01A) at the European Synchrotron Radiation Facility (ESRF), Grenoble, France. The diffraction data were collected in transmission mode (λ = 0.6999 Å) using the *PILATUS@SNBL* platform.[34] The experimental setup consisted of a single crystal sapphire capillary (1.15 ± 0.1 and 0.8 ± 0.08 mm outer and inner diameters, respectively) connected to a high-pressure liquid chromatography pump at one end and closed at the other end, and a heat blower was placed above the capillary as heat source, as previously described.[35-37] The blower was pointed towards the sample once desired temperature and pressure were reached and data collection was started. The slurries were gently ground in a mortar to facilitate injection in the capillary with a plastic syringe. Rietveld refinements were performed in batches using TOPAS (Bruker AXS version 5) operating in launch mode, and jEdit with macros for TOPAS.[38] More details about the diffraction data acquisition and analysis are given in the supporting information.

Scanning electron microscope (SEM) images were recorded on an in-lens cold field emission S(T)EM Hitachi S-5500. The acceleration voltage was 7 kV and secondary electrons were detected. Samples were prepared by dropping an aqueous suspension of the particles obtained after

the centrifugation on an aluminium sample holder, which was set to dry overnight. The linear intercept method was used to calculate average particle sizes, using images containing more than 100 particle intercepts.

Transmission electron microscope (TEM) images were recorded on a JEOL 2100 equipped with Oxford X-Max 80 SDD detector for energy-dispersive X-ray spectroscopy (EDS) analysis. The acceleration voltage was 200 kV. For the preparation of the TEM samples, the nanoparticles were dispersed in anhydrous propan-2-ol (Sigma-Aldrich, 99.5 %) dropped on a carbon coated copper TEM grid (Lacey). The high resolution TEM (HR-TEM) images were analyzed using DigitalMicrograph (Gatan Inc. version 3.01).

Specific surface area (Brunauer-Emmett-Teller (BET) method[39]) and pore size distribution (Barrett-Joyner-Halenda (BJH) method[40]) were measured by nitrogen adsorption on a Micrometrics Tristar 3000. Samples were degassed for 12 h at 180 °C in vacuum prior to analysis. Particle sizes were estimated from the specific surface area assuming non-porous and spherical particles.

Fourier transform infrared (FTIR) spectra were acquired on a Bruker Vertex 80v FTIR equipped with Bruker Platinum ATR diamond system from 600 to 4000 cm^{-1}. A total of 32 scans were acquired for each sample at a resolution of 1 cm^{-1}.

Thermogravimetric analysis (TGA) was acquired on a Netzsch Jupiter STA 449 C using an alumina crucible. The nanoparticles were firstly heat treated from 25 to 150 °C (10 °C min^{-1}), maintained at 150 °C for 30 min, cooled to room temperature, and heat treated again from 25 to 200 °C (2 °C min^{-1}) in order to remove adsorbed water. The samples were finally heat treated from 100 to 700 °C (2 °C min^{-1}). All treatments were performed under synthetic air.

3. RESULTS

3.1 Particle size, morphology, and functionalization

Selected SEM images of the nanoparticles are presented in Figure 1. The non-functionalized samples consist of particles with a size of about 10 nm. Significantly larger rod-like particles with lengths from 50 to 200 nm were formed for samples functionalized with APTES in addition to spherical nanoparticles. The average particle sizes are presented in Table 2. For the functionalized samples, shorter reaction time resulted in a smaller average particle (Figure S2 and Table S3 in supporting information), and basic reaction conditions promote the formation of rods, while acidic conditions considerably reduce the rod formation (Figure 1a-c). Sample 10:1-B consists of the largest and highest number of rod-like nanoparticles (Figures 1c and 2a). HR-TEM images of an [001] elongated single crystal from this sample is shown in Figure 2c. From the shape of this particle it is likely that at least two individual crystals have merged via oriented attachment mechanism since the curved surface at the center of the particle would be energetically unfavored during a conventional growth mechanism. Another typical single crystal rod-like anatase nanoparticle is displayed in Figure 2d, also presenting an elongation along the [001] crystallographic direction. The pH has negligible influence on the particle size and morphology in absence of the surface functionalization (Figure 1d-f).

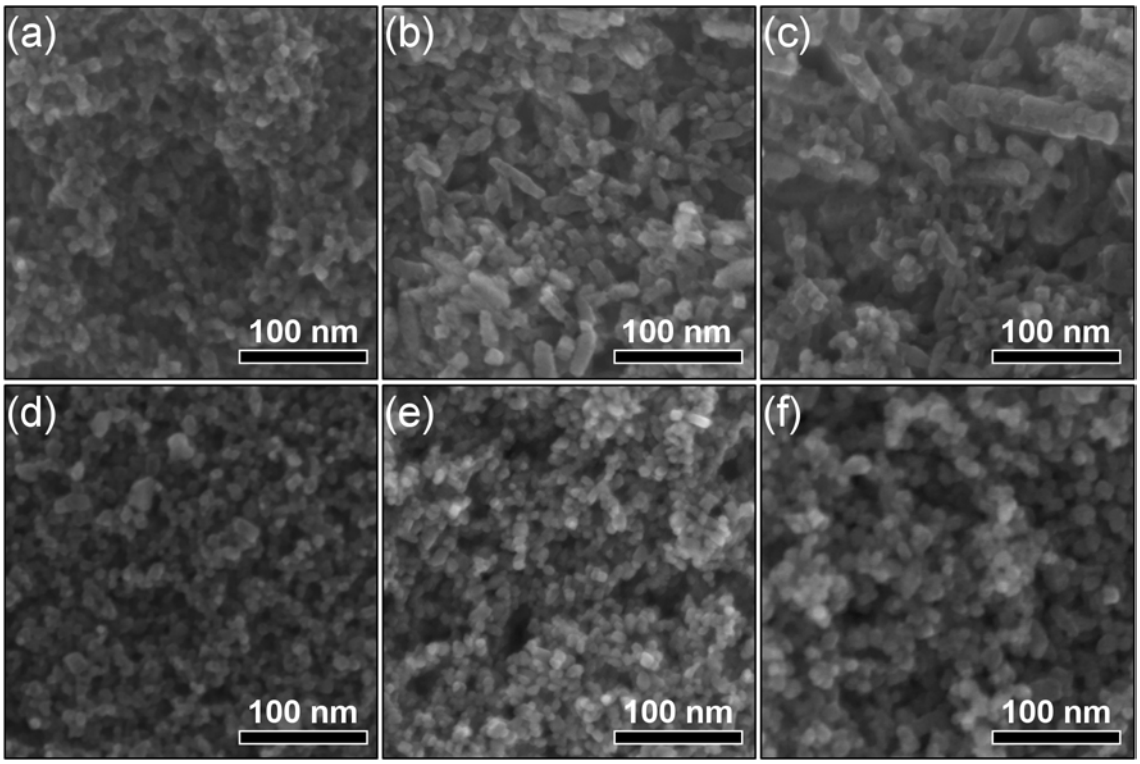

Figure 1. SEM micrographs of (a) 10:1-A, (b) 10:1, (c) 10:1-B, (d) TiO_2-A, (e) TiO_2, and (f) TiO_2-B samples.

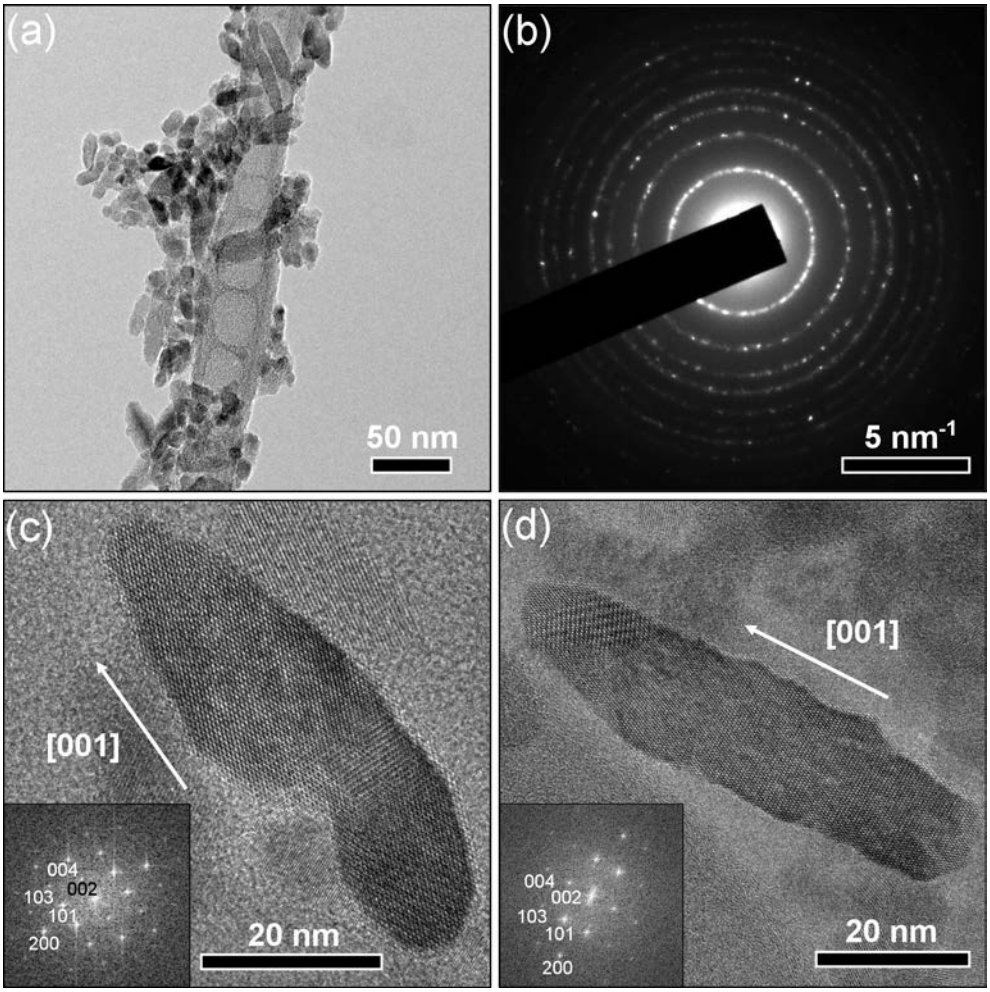

Figure 2. TEM images of 10:1-B sample: (a) overview (b) electron diffraction pattern assigned to anatase, (c) a rod-like nanoparticle formed from attached nanoparticles, (d) a rod-like nanoparticle; insets show fast Fourier transform of a selected area within the particle.

Table 2. Nanoparticle characteristics from nitrogen adsorption, XRD, SEM, and TGA analysis.

Sample	d_{XRD}[a] (nm)	d_{SEM}[c] (nm)	d_{BET}[b] (nm)	d_{BJH}[d] (nm)	S_{BET}[e] (m^2 g^{-1})	Organic mass loss (%)	Surface coverage (nm^{-2})
TiO_2-A	4.6 ± 0.1	7.9 ± 0.6	7.6 ± 0.1	7.3 ± 0.1	203 ± 1	n/a	n/a
TiO_2	4.8 ± 0.1	9.3 ± 0.1	9.0 ± 0.1	7.3 ± 0.1	171 ± 1	n/a	n/a
TiO_2-B	6.1 ± 0.1	9.1 ± 0.6	9.7 ± 0.1	5.7 ± 0.1	158 ± 1	n/a	n/a
10:1-A	5.9 ± 0.2	8.3 ± 0.5	8.7 ± 0.1	14.6 ± 0.1	177 ± 1	5.0 ± 0.5	2.9 ± 0.3
10:1	5.4 ± 0.1	11.6 ± 1.0	7.2 ± 0.1	11.3 ± 0.1	213 ± 1	8.2 ± 0.5	4.0 ± 0.3
10:1-B	8.4 ± 0.1	13.7 ± 3.0	6.3 ± 0.1	6.6 ± 0.1	243 ± 1	7.0 ± 0.5	3.0 ± 0.2
15:1-A	4.9 ± 0.1	10.0 ± 0.9	8.1 ± 0.1	6.6 ± 0.1	190 ± 1	3.4 ± 0.5	1.9 ± 0.3
15:1	5.5 ± 0.1	12.2 ± 1.2	8.5 ± 0.1	5.5 ± 0.1	182 ± 1	6.0 ± 0.5	3.4 ± 0.3
15:1-B	7.4 ± 0.1	10.5 ± 0.7	8.4 ± 0.1	8.0 ± 0.1	183 ± 1	5.1 ± 0.5	2.9 ± 0.3

[a] Average crystallite size from Rietveld refinement of XRD measurements.

[b] Particle size from SEM observations.

[c] Particle size estimated from BET specific surface area.

[d] Average pore diameter from BJH desorption calculations.

[e] BET specific surface area from nitrogen adsorption measurements.

Surface area and particle size calculated from BET specific surface area, as well as average pore size distribution from BJH desorption are included in Table 2 (Figure S2 in supporting information). The average particle sizes estimated from these measurements are in accordance with the size observed by SEM. The differences when comparing acidic or basic reaction conditions could be assigned to a different degree of agglomeration of the particles in these samples. The surface coverage (ranging from 1.7 to 4.0 silane nm^{-2}) was calculated from the mass loss measured during TGA analysis from 230 to 460 °C (Figure S3 in supporting information) and

BET specific surface area and are included in Table 2.[27] With respect to reaction time, the mass loss is fairly constant, but is considerably lower for the samples with 15:1 compared to 10:1 molar ratio (TIP:APTES). FTIR spectra confirm that APTES is covalently bonded to the surface of the nanoparticles via formation of Ti–O–Si bonds, and crosslinked at the surface of the particles via formation of Si–O–Si bonds (Figure S4 and Table S4 in supporting information).[9, 11, 27, 33] TEM analysis (Figures 2 and S5 in supporting information) does not show clear evidence of an amorphous coating, confirming the nanometric nature of the functionalization layer.

Surface energies calculated by DFT, given in Table 3, are in agreement with previously published results.[41, 42] These surface energies result in a square truncated bipyramid Wulff construction, replicating the known equilibrium anatase nanoparticle shape (Figure 3a).[43] The surface energy of all facets is lowered by APTES adsorption but the ratio of surface energies between the facets remains similar, such that the Wulff construction is not strongly changed (Figure 3b). This indicates that the equilibrium nanoparticle shape is not strongly affected by APTES adsorption. The (100) surfaces are not predicted to appear in the Wulff plots of either the bare surfaces or the APTES functionalized surfaces. The binding energy is positive and reasonably large for all three surfaces, indicating that APTES absorption is favorable and likely on all surfaces.

Table 3. Bare and APTES adsorbed surface energies, and binding energies of APTES to (001), (100) and (101) anatase surfaces.

	(001)	(100)	(101)
Bare surface energy (J m^{-2})	1.170	0.712	0.609
APTES adsorbed surface energy (J m^{-2})	0.567	0.400	0.338
Binding energy (eV)	2.145	1.413	1.315

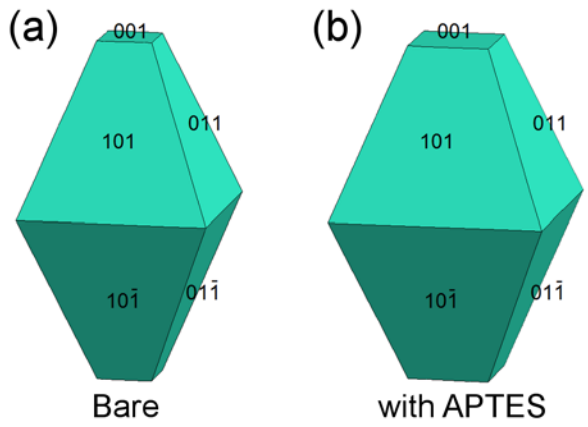

Figure 3. Wulff constructions of anatase nanoparticle shapes with (a) bare surfaces and (b) APTES adsorption, based on DFT calculated surface energies.

3.2 X-ray diffraction analysis

X-ray diffractograms presented in Figure 4a, show that all the functionalized samples are phase pure anatase. The non-functionalized samples are mainly anatase with 28, 22 and 14 wt. % brookite in acidic, neutral, and basic reaction conditions, respectively (Figure S6 in supporting information). In the case of *in situ* functionalized samples, the average crystallite sizes are found to be below 10 nm from the Rietveld refinements (Figure S7 in supporting information), and are included in Table 2. The small sizes are consistent with the broad reflections. The crystallite sizes decrease with decreasing reaction time (Table S3 in supporting information). For the samples functionalized with APTES, the (004) reflection is considerably narrower than the other reflections, pointing to anisotropic crystallite sizes due to the presence of the [001] oriented rod-like nanoparticles. Implementing anisotropic size broadening in the Rietveld refinements (see details in the supporting information) was necessary to improve the fit of all the diffractograms of functionalized nanoparticles as similarly done by Jensen *et al*., in the case of the synthesis of pure

TiO_2 in benzyl alcohol.[18] The anisotropic size broadening also allows to extract the average crystallite size (av. size) as well as the crystallite sizes along *a*-axis and *c*-axis of anatase ($size_a$ and $size_c$, respectively). The size anisotropy (expressed as a percentage) was calculated, as previously reported,[18] using Equation 1. It must be noted that the functionalized materials contain both spheres and rods, thus the size anisotropy also reflects the average of their respective contributions. The size anisotropy diminishes under acidic conditions, and increases when basic reaction conditions are used. This is also reflected in the refined crystallite sizes, where 10:1-B (having the narrowest (004) reflection) have the largest crystallite sizes and anisotropy (Figure 5). The crystallite sizes of 10:1 samples are larger than the 15:1 samples, at any pH condition.

$$\text{Size anisotropy} = \frac{\text{Size}_c - \text{Size}_a}{\text{Size}_c} \qquad (1)$$

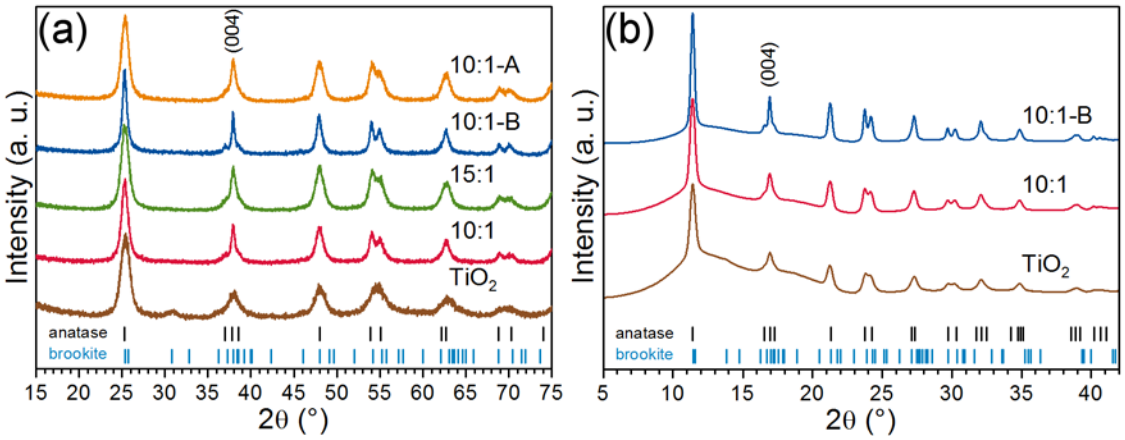

Figure 4. Normalized diffractograms collected (a) *ex situ* (λ = 1.5406 Å) and (b) *in situ* (λ = 0.6999 Å), at room temperature and after reaction (vertical bars show diffraction lines of anatase from ICDD card #00-021-1272 and brookite from ICDD card #00-029-1360).

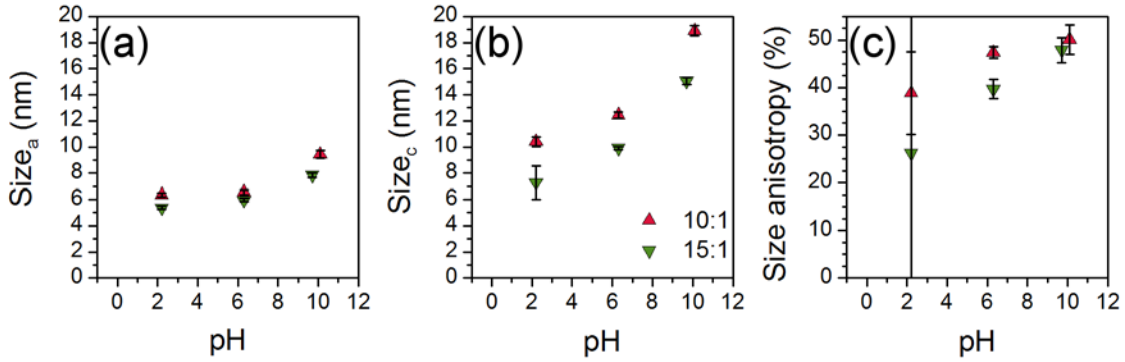

Figure 5. Crystallite sizes along the (a) *a*-axis and (b) *c*-axis, and (c) size anisotropy evolution as a function of the pH of the synthesis of 10:1 and 15:1 samples (from *ex situ* XRD).

The diffractograms of the final reaction products after cooling to room temperature are shown in Figure 4b. Table 4 summarizes the results from Rietveld refinements (Figure S8 in supporting information). The *in situ* synthesis of pure TiO_2 resulted in 13 wt.% brookite according to the Rietveld refinement, but the exactitude of the amount must be taken cautiously due to overlap with the solution background. The only distinguishable diffraction peak (121) is at 13.86°.

Table 4. Results of Rietveld refinements of long exposure diffractograms of end reaction products collected *in situ* at room temperature.

Sample	Duration of reaction (h)	R_{wp} (%)	Lattice parameters (Å)		Crystallite sizes (nm)			Size anisotropy (%)
			a	*c*	Av. size	Size$_a$	Size$_c$	
TiO_2	1.75	1.06	3.7991(3)	9.5130(9)	6.28(15)	6.29(12)	7.29(22)	14 ± 7
10:1	1.58	1.03	3.7977(2)	9.5204(5)	7.44(11)	7.22(9)	9.11(17)	21 ± 2
10:1-B	9[a]	1.87	3.7969(1)	9.5236(4)	10.20(14)	9.52(12)	14.11(27)	32 ± 1

[a] Limited evolution after about 100 min of reaction.

The XRD contour plots of the first 40 min of the reactions of the three syntheses are displayed in Figure 6. Nucleation of anatase occurs rapidly, within tens of seconds after the initial heating, without the formation of any intermediate phase. The broadening of the reflections is largest for pure TiO_2 (Figure 6a), reflecting a smaller crystallite size. The size broadening is smaller when the synthesis is performed with APTES (Figure 6b), and even smaller with APTES in basic conditions (Figure 6c). This reduction in the broadening is also visible from Figure 7 which shows the initial 15 min evolution of the (004) (*c*-parameter) and (200) (*a*-parameter) reflections.

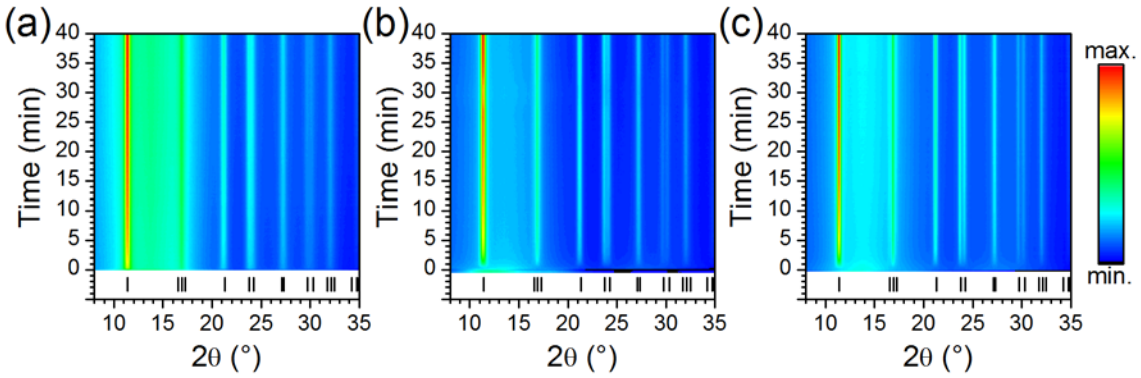

Figure 6. Time resolved XRD contour plots (λ = 0.6999 Å) of (a) TiO_2, (b) 10:1, and (c) 10:1-B samples collected during the syntheses at 213 °C and 250 bars (the color scale represents the intensity and the vertical bars show diffraction lines of anatase from ICDD card #00-021-1272).

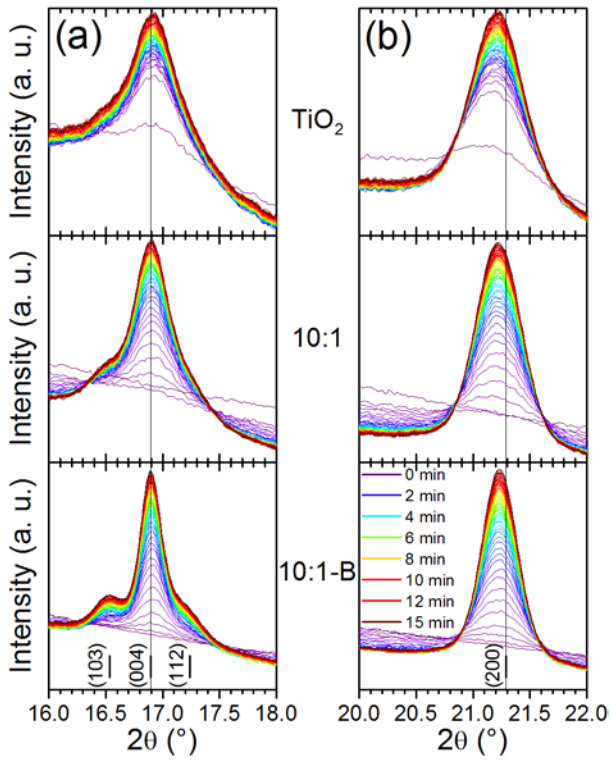

Figure 7. Time evolution of (a) (004) and (b) (200) diffraction lines (λ = 0.6999 Å) during the first 15 min of the hydrothermal synthesis of TiO_2 (top), 10:1 (middle), and 10:1-B (bottom) samples (vertical bars show recalculated bulk diffraction line positions of anatase at 213 °C).

The relative full width at half maximum of the (004) and (200) reflections in Figure 7 reveals the anisotropic growth of the particles when the synthesis is performed with APTES, particularly at basic conditions. Figure 8 shows crystallite sizes along the anatase cell parameter directions and the size anisotropy as a function of time from the diffraction data refinements. The crystal growth occurs within the first minutes of reaction and increases continuously for the growth along the *a*-axis. The size difference is larger along the *c*-axis in the case of APTES functionalized samples. Two phases of growth are distinguishable (separated at about 5 minutes of reaction). The growth rate of the crystallite size along the *c*-axis decreases more rapidly than the one along the *a*-axis.

Thus, the size anisotropy is evident from the initial moments of the reactions and reach a maximum of 38 % and 26 % for 10:1-B and 10:1 samples, respectively, and decreases constantly to reach the values reported in Table 4. The same trends are observed in the case of *ex situ* analysis (Figure S9 in supporting information), but the calculated size anisotropy is larger (up to 48 %) even though the pH was not modified. The size anisotropy is more pronounced in the case of 10:1 samples than the 15:1 samples.

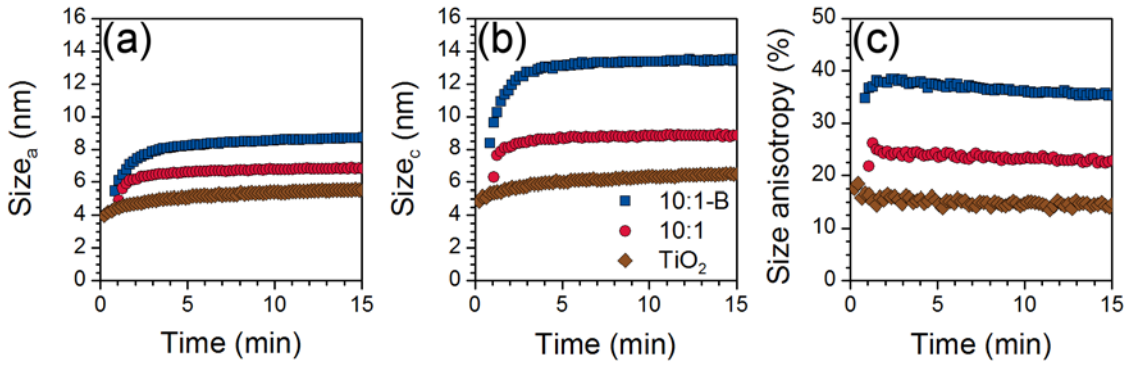

Figure 8. Time evolution of the crystallite sizes along the (a) *a*-axis and (b) *c*-axis, and (c) size anisotropy from *in situ* XRD.

The time evolution of the cell parameters is reported Figure 9. The *a*-parameter converges rapidly during the *in situ* measurements to 3.802 Å (slightly above in the case of pure TiO_2), via expansion (10:1) and contraction (TiO_2 and 10:1-B). In all cases, the *c*-parameter increases, but it remains well below the bulk value in the case of TiO_2, and it converges rapidly to values above calculated bulk value at 213 °C (9.535 Å and 9.539 Å for 10:1 and 10:1-B samples, respectively). Similar evolutions were also observed in previous studies of pure TiO_2.[44, 45] The divergence of the cell parameters from the bulk values during *in situ* XRD is also visible from the position of the

(004) and (200) Bragg reflections in Figure 7. The cell parameters for the pure TiO_2 nano-crystalline sample diverges the most from bulk TiO_2. These observations are contrasted with the *ex situ* measurements (Figure S10 in supporting information), where the *a*-parameter converges slowly to the bulk value via contraction, and the *c*-parameter expands but remains well below the bulk value, for both TIP:APTES ratios. However, in all cases, the *c*/*a* ratio shows similar trend, increasing and stabilizing at values below the bulk values.

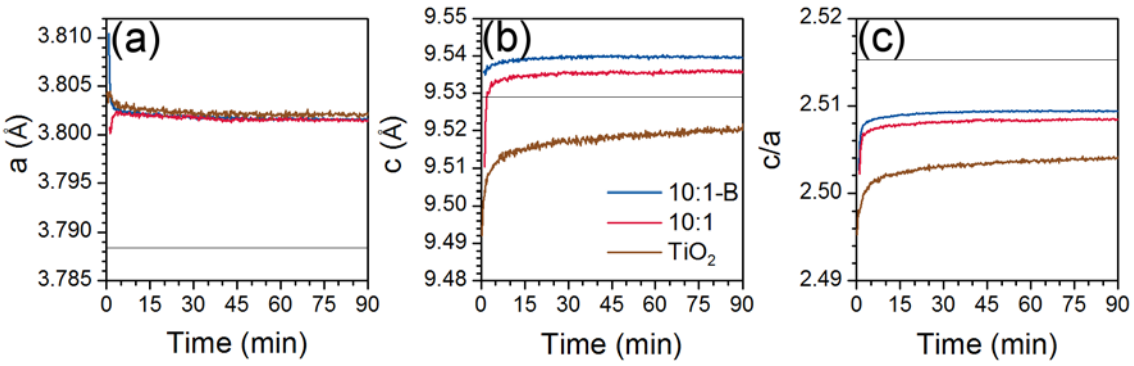

Figure 9. Time evolution of the (a) *a*-parameter, (b) *c*-parameter, and (c) *c*/*a* from *in situ* XRD (horizontal lines show bulk references of anatase recalculated at 213 °C).

4. DISCUSSION

The similarity of the diffractograms from the *ex situ* and *in situ* measurements (Figure 4) provides solid evidence of the robustness and the reproducibility of the synthesis conditions which can be reliably reproduced *in situ*. The *in situ* measurements are hence not biased and can be considered as representative for the reaction pathways.

In the case of pure TiO_2, the amount of brookite decreased when the pH was increased as previously observed.[46, 47] Nanoparticles of about 10 nm in size were obtained for all TiO_2 samples

(Figure 1c-e). From the SEM images, the morphology was not affected in contrast to previous hydrothermal studies where a strong dependence of the particles morphology with pH was reported, often leading to elongated nanoparticles in basic conditions.[20, 21, 48] With respect to the cell parameters and crystallite size, the values reported here follow the trend from previously reported *in situ* studies of hydrothermal synthesis of TiO_2 at different temperatures.[45] The kinetics of the crystallite growth (Figure 8a-b) follows a power-law type of function (Equation 2), where d is the crystallite size at the time t, d_0 is the average size at $t = 0$, k_{OR} is a temperature-dependent rate constant, and n is an integer exponent when the growth can be attributed to Ostwald ripening mechanism.[49, 50] The fitted parameters using Equation 2 on the crystallite size of TiO_2 during *in situ* XRD measurements are available in Table 5 and the fitted plots in Figure S11 in supporting information. The best fits were obtained for $n = 4$, indicating that growth is controlled by dissolution kinetics at the particle-matrix interface.[50]

$$d - d_0 = k_{OR} t^{1/n} \qquad (2)$$

When TiO_2 nanoparticles are *in situ* functionalized with APTES, the differences in phase purity, morphology and growth mechanisms are attributed to APTES, as the conditions were the same as during the synthesis performed without APTES. The differences result from a combination of several effects, since the growth and the functionalization of the nanoparticles occur simultaneously. The nucleation of the TiO_2 nanoparticles is most likely to occur first due to the much higher reactivity of titanium alkoxides compared to their silicon counterparts in aqueous media.[51] After nucleation, as the binding energy of APTES is large and positive (> 1.3 eV) for all facets (Table 3), aminosilanes probably adsorb regardless of facet. The similarity in nanoparticle shape predicted by DFT with and without APTES adsorption (Figure 3) supports the theory that oriented attachment is occurring. This differs from the pH affect shown by Barnard *et al.*[43], where

the surface energy of the (100) faces is lowered by highly basic conditions and the shape of the nanoparticles is elongated along the *c*-axis. Such a result would support a preferential growth mechanism. In the case shown here, however, the surface energy of the (100) faces remains too high to be stable, hence preferential growth is not favored, and a relative roughness of the surfaces parallel to the elongation direction can be observed in Figure 2d. The adsorption of APTES provides the building blocks for oriented attachment mechanism reaction (Figure 2c), within the few first minutes of the synthesis. Yet, the highest binding energy is on the (001) faces, which are also the faces with the highest surface energy (Table 3), so if there is preferential adsorption of APTES on the (001) faces then this would likely attract the nanoparticles in this direction due to the polarity effect (hydrogen bonding of amino groups and hydrophobicity of the silanes), causing oriented attachment along the *c*-axis. Attraction of the building blocks facing (001) facets could desorb APTES molecules, increasing the total entropy of the system and providing the alignment of the nanoblocks for oriented attachment. Thus, the anisotropy of the particle along the preferential [001] or *c*-axis (Figures 2c-d and Figure 8) is observed. At longer reaction time, crosslinking of APTES on the surface of the nanoparticles (which is kinetically slower than the growth of the particles, see Si–O–Si FTIR band intensity as a function of the time in Figure S4 in supporting information) does not allow for more drastic changes in the nanoparticle morphology. These competing phenomena (growth and functionalization) result in the mixture of spheres and rods. On the other hand, the role of APTES is also demonstrated when the amount is reduced (15:1 samples) leading to reduced amount and size of rod-like nanoparticles. During the second phase of the growth, when a slower evolution of the cell parameters and crystallite sizes is observed, ongoing crosslinking of APTES on the surface of the nanoparticles prevents further growth of the particles along the *c*-axis. However, surface diffusion might still occur to reach an equilibrium

morphology (Figure 3b), thus the slow increase of the crystallite size along the *a*-axis and the slow decrease of the anisotropy (Figure 8c) resulting in partially faceted nanorods (Figure 2c-d). To confirm, the *in situ* diffractogram of 10:1-B (Figure 4b) was taken after 9 h of reaction and limited evolution was observed after about 100 min of reaction.

The kinetics of crystallite growth of the functionalized samples, for both *in situ* (Figure 8a-b) and *ex situ* data (Figure S9 in supporting information), could not be fitted to a power-law type of function as presented in Equation 2. However, the fitting could be done using Equation 3, describing an oriented attachment mechanism, where *m* was defined as the aggregation factor and k_{OA} the rate constant for oriented attachment.[52] The fitted parameters using Equation 3 for the growth of the functionalized nanoparticles are available in Table 5 (see Table S5 and Figure S11 in supporting information for *ex situ* XRD data and fitted plots). The rate of growth of pure TiO_2 is similar in both crystallographic directions while in the case of functionalized samples, the rate of growth along the *c*-axis is 2 to 4 times higher than along the *a*-axis, depending on the synthesis conditions. Additionally, it can be observed that the aggregation factor is also more important along the *c*-axis and increases when increasing pH and APTES values. These observations are consistent with electron microscope observations (Figures 1 and 2).

$$d = d_0 \frac{1 + m k_{OA} t}{1 + k_{OA} t} \qquad (3)$$

Table 5. Fitted parameters for the kinetics of crystallite growth obtained from *in situ* XRD.

Sample	Variable	d_0 (nm)	k_{OR} (nm $min^{-1/n}$)	k_{OA} (min^{-1})	m	R^2
TiO_2	$Size_a$	3.9	0.80	n/a	n/a	0.98
	$Size_c$	4.6	0.95	n/a	n/a	0.98
10:1	$Size_a$	4.3	n/a	0.65	1.7	0.81
	$Size_c$	2.7	n/a	2.55	3.3	0.66
10:1-B	$Size_a$	3.9	n/a	0.77	2.4	0.97
	$Size_c$	2.2	n/a	2.60	6.3	0.88

The functionalization of the TiO_2 nanoparticles increases the stability of the nanoparticles by reducing the deviation from the bulk of the cell parameters (Figure 9b), and results in phase pure anatase TiO_2. Functionalization of the nanoparticles reduces the finite size effect which is usually observed for anatase nanoparticles,[53, 54] by creating covalent bonds with the silane coupling agent (passivation of the dangling bonds), reducing the surface stress and surface energy of the nanoparticles (Table 3). The variations of the cell parameters as a function of the pH are relatively small thus the difference in the particle size does not seem to be the origin of this difference between pure TiO_2 and the *in situ* functionalized sample. However, the variations of pH towards more acidic or more basic conditions strongly influence the anisotropy (Figure 1a-c). The surface state of TiO_2 nanoparticles, the attractive forces, and the reactivity of titanium alkoxides and silane coupling agents are affected by the variations of the pH. A more homogeneous system and a kinetically faster functionalization (increasing the extent of crosslinking that can be achieved before oriented attachment takes place) would lead towards more spherically shaped nanoparticles. These observations justify previous results in which *in situ* functionalization of TiO_2 with *n*-

decyltriethoxysilane (non-polar) and 3-(2-aminoethylamino)propyldimethoxymethylsilane (two amino groups) resulted in the observations of only spheres, and a mixture of spheres and larger rods (compared to functionalization with APTES), respectively.[27]

To summarize, in the case of the hydrothermal synthesis of TiO_2, a classical Ostwald ripening process was observed (Figure 10a). When APTES was introduced (Figure 10b), the adsorption of the aminosilane coupling agent favors the anatase polymorph and an oriented attachment process is observed via the anisotropic broadening of the Bragg reflections, HR-TEM imaging, kinetic modelling, and DFT calculations. Functionalization and crosslinking of APTES on the surface of TiO_2 nanoparticles also contributes to reduce the rate of growth at longer reaction times.

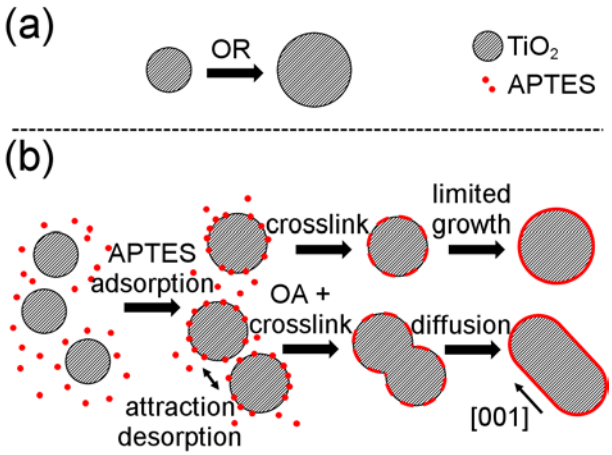

Figure 10. Schematics of the growth processes during the hydrothermal synthesis of (a) TiO_2 and (b) TiO_2 *in situ* functionalized with APTES (OR: Ostwald ripening, OA: oriented attachment).

5. CONCLUSION

The effect of pH, precursor/functionalization agent ratio, and time during the hydrothermal synthesis of TiO_2 and APTES functionalized TiO_2 was investigated in detail by *ex situ* and *in situ*

techniques. While nanoparticles of about 10 nm in size were obtained for pure TiO_2, additional [001] oriented rod-like nanoparticles were formed due to an oriented attachment mechanism in presence of APTES. The amount and the size of the rod-like nanoparticles was shown to increase with increasing pH, and decrease with a lower amount of APTES. Comparison of *ex situ* and *in situ* XRD showed that the *in situ* results were representative for the reaction. *In situ* XRD allowed to follow the growth kinetics of the synthesis, despite the extreme conditions of the synthesis (213 °C and 250 bar). DFT calculations supported an oriented attachment mechanism as elongated nanoparticle was shown to not be the stable shape after functionalization. The hydrothermal synthesis of functionalized TiO_2 has the main advantage of being a single-step method, and understanding the phenomenon and the reaction processes are essential in order to gain control over the product of the synthesis. This method opens further possibilities for green synthesis of *in situ* functionalized nano oxides with desired size, shape, phase, and surface properties.

ASSOCIATED CONTENT

Supporting Information

Experimental details for *in situ* diffraction analysis and Rietveld refinement, detailed computational calculations description, *ex situ* analysis on the synthesis time, nitrogen adsorption and desorption isotherms, BJH pore size distribution, thermogravimetry data, Fourier transform infrared spectra, additional HR-TEM images and EDS spectrum, Rietveld fits, time evolution of parameters from *ex situ* XRD, and kinetic fits (PDF file).

AUTHOR INFORMATION

Corresponding Author

* Corresponding author: Mari-Ann Einarsrud

Email address: mari-ann.einarsrud@ntnu.no

Telephone: +47 73 59 40 02.

Notes

The authors declare no competing financial interest.

ACKNOWLEDGMENT

Financial support from the Research Council of Norway to the project "Beat the Human Eye" (number 235210) and for the support to NTNU NanoLab through the Norwegian Micro- and Nano-Fabrication Facility, NorFab (197411/V30), is gratefully acknowledged. KI and SMS were supported by NTNU and the Research Council of Norway through project number 240466/F20. Computational resources were provided by Sigma2 Uninett, through the project nn9264k. We acknowledge SNBL at ESRF, Grenoble, France for the granted beamtime. The TEM work was carried out on the NORTEM JEOL 2100 instrument, TEM Gemini Centre, NTNU, Norway, and we want to acknowledge Dr. Ragnhild Sæterli for help in operating the TEM. Dr. Julian R. Tolchard (SINTEF Materials and Chemistry) is acknowledged for the help with the Rietveld analysis.

REFERENCES

(1) Zhang, Y.; Jiang, Z.; Huang, J.; Lim, L. Y.; Li, W.; Deng, J.; Gong, D.; Tang, Y.; Lai, Y.; Chen, Z. Titanate and Titania Nanostructured Materials for Environmental and Energy Applications: A Review. *RSC Adv.* **2015**, *5*, 79479–79510.

(2) Liu, G.; Yang, H. G.; Pan, J.; Yang, Y. Q.; Lu, G. Q.; Cheng, H. M. Titanium Dioxide Crystals with Tailored Facets. *Chem. Rev.* **2014**, *114*, 9559–9612.

(3) Rabenau, A. The Role of Hydrothermal Synthesis in Preparative Chemistry. *Angew. Chem. Int. Ed.* **1985**, *24*, 1026–1040.

(4) Li, X.; Zheng, W.; He, G.; Zhao, R.; Liu, D. Morphology Control of TiO_2 Nanoparticle in Microemulsion and Its Photocatalytic Property. *ACS Sustainable Chem. Eng.* **2013**, *2*, 288–295.

(5) Bian, Z.; Zhu, J.; Li, H. Solvothermal Alcoholysis Synthesis of Hierarchical TiO_2 with Enhanced Activity in Environmental and Energy Photocatalysis. *J. Photochem. Photobiol. C* **2016**, *28*, 72–86.

(6) Lekphet, W.; Ke, T.-C.; Su, C.; Kathirvel, S.; Sireesha, P.; Akula, S. B.; Li, W.-R. Morphology Control Studies of TiO_2 Microstructures Via Surfactant-Assisted Hydrothermal Process for Dye-Sensitized Solar Cell Applications. *Appl. Surf. Sci.* **2016**, *382*, 15–26.

(7) Einarsrud, M.-A.; Grande, T. 1D Oxide Nanostructures from Chemical Solutions. *Chem. Soc. Rev.* **2014**, *43*, 2187–2199.

(8) Fadeev, A. Y.; Helmy, R.; Marcinko, S. Self-Assembled Monolayers of Organosilicon Hydrides Supported on Titanium, Zirconium, and Hafnium Dioxides. *Langmuir* **2002**, *18*, 7521–7529.

(9) Milanesi, F.; Cappelletti, G.; Annunziata, R.; Bianchi, C. L.; Meroni, D.; Ardizzone, S. Siloxane−TiO_2 Hybrid Nanocomposites. The Structure of the Hydrophobic Layer. *J. Phys. Chem. C* **2010**, *114*, 8287–8293.

(10) Chen, Q.; Yakovlev, N. L. Adsorption and Interaction of Organosilanes on TiO_2 Nanoparticles. *Appl. Surf. Sci.* **2010**, *257*, 1395–1400.

(11) Zhao, J.; Milanova, M.; Warmoeskerken, M. M. C. G.; Dutschk, V. Surface Modification of TiO_2 Nanoparticles with Silane Coupling Agents. *Colloids Surf., A* **2012**, *413*, 273–279.

(12) Plodinec, M.; Gajović, A.; Iveković, D.; Tomašić, N.; Zimmermann, B.; Macan, J.; Haramina, T.; Su, D. S.; Willinger, M. Study of Thermal Stability of (3-Aminopropyl)Trimethoxy Silane-Grafted Titanate Nanotubes for Application as Nanofillers in Polymers. *Nanotechnology* **2014**, *25*, 435601.

(13) Iijima, M.; Kobayakawa, M.; Kamiya, H. Tuning the Stability of TiO_2 Nanoparticles in Various Solvents by Mixed Silane Alkoxides. *J. Colloid Interface Sci.* **2009**, *337*, 61–65.

(14) Faure, B.; Salazar-Alvarez, G.; Ahniyaz, A.; Villaluenga, I.; Berriozabal, G.; De Miguel, Y. R.; Bergström, L. Dispersion and Surface Functionalization of Oxide Nanoparticles for Transparent Photocatalytic and UV-Protecting Coatings and Sunscreens. *Sci. Tech. Adv. Mater.* **2013**, *14*, 023001.

(15) Kango, S.; Kalia, S.; Celli, A.; Njuguna, J.; Habibi, Y.; Kumar, R. Surface Modification of Inorganic Nanoparticles for Development of Organic–Inorganic Nanocomposites—a Review. *Prog. Polym. Sci.* **2013**, *38*, 1232–1261.

(16) Dinh, C. T.; Nguyen, T. D.; Kleitz, F.; Do, T. O. Shape-Controlled Synthesis of Highly Crystalline Titania Nanocrystals. *ACS Nano* **2009**, *3*, 3737–3743.

(17) Jun, Y. W.; Casula, M. F.; Sim, J. H.; Kim, S. Y.; Cheon, J.; Alivisatos, A. P. Surfactant-Assisted Elimination of a High Energy Facet as a Means of Controlling the Shapes of TiO_2 Nanocrystals. *J. Am. Chem. Soc.* **2003**, *125*, 15981–15985.

(18) Jensen, G. V.; Bremholm, M.; Lock, N.; Deen, G. R.; Jensen, T. R.; Iversen, B. B.; Niederberger, M.; Pedersen, J. S.; Birkedal, H. Anisotropic Crystal Growth Kinetics of Anatase TiO_2 Nanoparticles Synthesized in a Nonaqueous Medium. *Chem. Mater.* **2010**, *22*, 6044–6055.

(19) Darbandi, M.; Dickerson, J. H. Nanoscale Engineering of TiO_2 Nanoparticles: Evolution of the Shape, Phase, Morphology, and Facet Orientation. *Mater. Lett.* **2016**, *180*, 212–218.

(20) Sugimoto, T.; Zhou, X.; Muramatsu, A. Synthesis of Uniform Anatase TiO_2 Nanoparticles by Gel–Sol Method 3. Formation Process and Size Control. *J. Colloid Interface Sci.* **2003**, *259*, 43–52.

(21) Sugimoto, T.; Zhou, X.; Muramatsu, A. Synthesis of Uniform Anatase TiO_2 Nanoparticles by Gel–Sol Method 4. Shape Control. *J. Colloid Interface Sci.* **2003**, *259*, 53–61.

(22) Penn, R. L.; Banfield, J. F. Imperfect Oriented Attachment: Dislocation Generation in Defect-Free Nanocrystals. *Science* **1998**, *281*, 969–971.

(23) Niederberger, M.; Cölfen, H. Oriented Attachment and Mesocrystals: Non-Classical Crystallization Mechanisms Based on Nanoparticle Assembly. *Phys. Chem. Chem. Phys.* **2006**, *8*, 3271–3287.

(24) Penn, R. L.; Banfield, J. F. Morphology Development and Crystal Growth in Nanocrystalline Aggregates under Hydrothermal Conditions: Insights from Titania. *Geochim. Cosmochim. Acta* **1999**, *63*, 1549–1557.

(25) Polleux, J.; Pinna, N.; Antonietti, M.; Niederberger, M. Ligand-Directed Assembly of Preformed Titania Nanocrystals into Highly Anisotropic Nanostructures. *Adv. Mater.* **2004**, *16*, 436–439.

(26) Dalmaschio, C. J.; Leite, E. R. Detachment Induced by Rayleigh-Instability in Metal Oxide Nanorods: Insights from TiO_2. *Cryst. Growth Des.* **2012**, *12*, 3668–3674.

(27) Dalod, A. R. M.; Henriksen, L.; Grande, T.; Einarsrud, M.-A. Functionalized TiO_2 Nanoparticles by Single-Step Hydrothermal Synthesis: The Role of the Silane Coupling Agents. *Beilstein J. Nanotechnol.* **2017**, *8*, 304–312.

(28) Kresse, G.; Hafner, J. Ab Initio Molecular Dynamics for Liquid Metals. *Phys. Rev. B* **1993**, *47*, 558–561.

(29) Kresse, G.; Furthmüller, J. Efficiency of Ab-Initio Total Energy Calculations for Metals and Semiconductors Using a Plane-Wave Basis Set. *Comput. Mater. Sci.* **1996**, *6*, 15–50.

(30) Kresse, G.; Furthmüller, J. Efficient Iterative Schemes for Ab Initio Total-Energy Calculations Using a Plane-Wave Basis Set. *Phys. Rev. B* **1996**, *54*, 11169–11186.

(31) Kresse, G.; Joubert, D. From Ultrasoft Pseudopotentials to the Projector Augmented-Wave Method. *Phys. Rev. B* **1999**, *59*, 1758–1775.

(32) Perdew, J. P.; Ruzsinszky, A.; Csonka, G. I.; Vydrov, O. A.; Scuseria, G. E.; Constantin, L. A.; Zhou, X.; Burke, K. Restoring the Density-Gradient Expansion for Exchange in Solids and Surfaces. *Phys. Rev. Lett.* **2008**, *100*, 136406.

(33) Meroni, D.; Lo Presti, L.; Di Liberto, G.; Ceotto, M.; Acres, R. G.; Prince, K. C.; Bellani, R.; Soliveri, G.; Ardizzone, S. A Close Look at the Structure of the TiO_2-APTES Interface in Hybrid Nanomaterials and Its Degradation Pathway: An Experimental and Theoretical Study. *J. Phys. Chem. C* **2017**, *121*, 430–440.

(34) Dyadkin, V.; Pattison, P.; Dmitriev, V.; Chernyshov, D. A New Multipurpose Diffractometer PILATUS@SNBL. *J. Synchrotron Radiat.* **2016**, *23*, 825–829.

(35) Becker, J.; Bremholm, M.; Tyrsted, C.; Pauw, B.; Jensen, K. M. Ø.; Eltzholt, J.; Christensen, M.; Iversen, B. B. Experimental Setup for in situ X-Ray SAXS/WAXS/PDF Studies of the Formation and Growth of Nanoparticles in near- and Supercritical Fluids. *J. Appl. Crystallogr.* **2010**, *43*, 729–736.

(36) Jensen, K. M.; Christensen, M.; Juhas, P.; Tyrsted, C.; Bojesen, E. D.; Lock, N.; Billinge, S. J.; Iversen, B. B. Revealing the Mechanisms Behind SnO_2 Nanoparticle Formation and Growth During Hydrothermal Synthesis: An in situ Total Scattering Study. *J. Am. Chem. Soc.* **2012**, *134*, 6785–6792.

(37) Skjærvø, S. L.; Sommer, S.; Nørby, P.; Bøjesen, E. D.; Grande, T.; Iversen, B. B.; Einarsrud, M.-A. Formation Mechanism and Growth of MNbO3, M=K, Na by in situ X-Ray Diffraction. *J. Am. Ceram. Soc.* **2017**, doi: 10.1111/jace.14932, in press.

(38) Evans, J. S. O. Advanced Input Files & Parametric Quantitative Analysis Using Topas. *Mater. Sci. Forum* **2010**, *651*, 1–9.

(39) Brunauer, S.; Emmett, P. H.; Teller, E. Adsorption of Gases in Multimolecular Layers. *J. Am. Chem. Soc.* **1938**, *60*, 309–319.

(40) Barrett, E. P.; Joyner, L. G.; Halenda, P. P. The Determination of Pore Volume and Area Distributions in Porous Substances. I. Computations from Nitrogen Isotherms. *J. Am. Chem. Soc.* **1951**, *73*, 373–380.

(41) Zhao, Z.; Li, Z.; Zou, Z. Surface Properties and Electronic Structure of Low-Index Stoichiometric Anatase TiO_2 Surfaces. *J. Phys.: Condens. Matter* **2010**, *22*, 175008.

(42) Martsinovich, N.; Troisi, A. How TiO_2 Crystallographic Surfaces Influence Charge Injection Rates from a Chemisorbed Dye Sensitiser. *Phys. Chem. Chem. Phys.* **2012**, *14*, 13392–13401.

(43) Barnard, A. S.; Curtiss, L. A. Prediction of TiO_2 Nanoparticle Phase and Shape Transitions Controlled by Surface Chemistry. *Nano Lett.* **2005**, *5*, 1261–1266.

(44) Mi, J.-L.; Jensen, K. M. Ø.; Tyrsted, C.; Bremholm, M.; Iversen, B. B. In Situ Total X-Ray Scattering Study of the Formation Mechanism and Structural Defects in Anatase TiO_2 Nanoparticles under Hydrothermal Conditions. *CrystEngComm* **2015**, *17*, 6868–6877.

(45) Eltzholtz, J. R.; Tyrsted, C.; Ornsbjerg Jensen, K. M.; Bremholm, M.; Christensen, M.; Becker-Christensen, J.; Iversen, B. B. Pulsed Supercritical Synthesis of Anatase TiO_2

Nanoparticles in a Water-Isopropanol Mixture Studied by in situ Powder X-Ray Diffraction. *Nanoscale* **2013**, *5*, 2372–2378.

(46) Reyes-Coronado, D.; Rodríguez-Gattorno, G.; Espinosa-Pesqueira, M. E.; Cab, C.; de Coss, R.; Oskam, G. Phase-Pure TiO_2 Nanoparticles: Anatase, Brookite and Rutile. *Nanotechnology* **2008**, *19*, 145605.

(47) Zhang, H.; Banfield, J. F. Structural Characteristics and Mechanical and Thermodynamic Properties of Nanocrystalline TiO_2. *Chem. Rev.* **2014**, *114*, 9613–9644.

(48) Ribeiro, C.; Barrado, C. M.; de Camargo, E. R.; Longo, E.; Leite, E. R. Phase Transformation in Titania Nanocrystals by the Oriented Attachment Mechanism: The Role of the pH Value. *Chem. Eur. J.* **2009**, *15*, 2217–2222.

(49) Xue, X.; Penn, R. L.; Leite, E. R.; Huang, F.; Lin, Z. Crystal Growth by Oriented Attachment: Kinetic Models and Control Factors. *CrystEngComm* **2014**, *16*, 1419–1429.

(50) Huang, F.; Zhang, H.; Banfield, J. F. Two-Stage Crystal-Growth Kinetics Observed During Hydrothermal Coarsening of Nanocrystalline ZnS. *Nano Lett.* **2003**, *3*, 373–378.

(51) Rozes, L.; D'Arras, L.; Hoffman, C.; Potier, F.; Halttunen, N.; Nicole, L. In *Chemistry of Organo-Hybrids: Synthesis and Characterization of Functional Nano-Objects*; Charleux, B., Copéret, C., Lacôte, E., Eds.; John Wiley & Sons: Hoboken, NJ, USA, 2015; pp 114–167.

(52) Zhan, H.; Yang, X.; Wang, C.; Liang, C.; Wu, M. Multiple Growth Stages and Their Kinetic Models of Anatase Nanoparticles under Hydrothermal Conditions. *J. Phys. Chem. C* **2010**, *114*, 14461–14466.

(53) Ahmad, M. I.; Bhattacharya, S. S. Size Effect on the Lattice Parameters of Nanocrystalline Anatase. *Appl. Phys. Lett.* **2009**, *95*, 191906.

(54) Zhang, H.; Chen, B.; Banfield, J. F. The Size Dependence of the Surface Free Energy of Titania Nanocrystals. *Phys. Chem. Chem. Phys.* **2009**, *11*, 2553–2558.

TOC graphic